PNAS NEXUS

PNAS Nexus, 2025, 4, pgaf153
https://doi.org/10.1093/pnasnexus/pgaf153
Advance access publication 9 May 2025
Research Report

Perfluorinated compounds exposure and atherogenic risk characteristics in a high-fat diet condition: In vitro/in vivo models and population panel study

Ziyuan Li[a,1], Ze Zhang[a,1], Biao Zhang[b,1], Chengying Zhou[a,1], Hongyan Yu[a], Liting Xu[a], Zhicong He[c], Pu Chen[a], Wei Peng[d], Mingliang Ye[e], Guangbo Qu[f], Xiaomin Zhang[b,*], Yang Song[f,*], Xiaoting Jin[a,*] and Yuxin Zheng[a]

[a]Department of Occupational Health and Environmental Health, School of Public Health, Qingdao University, Qingdao 266071, China
[b]Department of Occupational and Environmental Health, Ministry of Education Key Laboratory of Environment and Health, and State Key Laboratory of Environmental Health (Incubating), School of Public Health, Tongji Medical College, Huazhong University of Science and Technology, Wuhan 430030, China
[c]School of Water and Environment, Key Laboratory of Subsurface Hydrology and Ecological Effect in Arid Region of Ministry of Education, Key Laboratory of Ecohydrology and Water Security in Arid and Semi-Arid Regions of Ministry of Water Resources, Chang' an University, Xi'an 710054, China
[d]Key Laboratory of Aerosol Chemistry and Physics, State Key Laboratory of Loess and Quaternary Geology, Institute of Earth Environment, Chinese Academy of Sciences (CAS), Xi'an 710061, China
[e]CAS Key Laboratory of Separation Science for Analytical Chemistry, Dalian Institute of Chemical Physics, Chinese Academy of Sciences, Dalian 116023, China
[f]State Key Laboratory of Environmental Chemistry and Ecotoxicology, Research Center for Eco-Environmental Sciences, Chinese Academy of Sciences, Beijing 100085, China
*To whom correspondence should be addressed: Email: mingxz117@163.com (X.Z.); Email: yangsong@rcees.ac.cn (Y.S.); Email: xtjin@qdu.edu.cn (X.J.)
[1]These authors contributed equally to this work.
Edited By Rebecca Seguin-Fowler

Abstract

Perfluorinated compounds (PFCs) are a well-recognized environmental risk factor for atherosclerosis. However, corresponding atherogenic risk in susceptible populations consuming high-fat diets (HFDs) remains unclear. Here, we found that perfluorooctane sulfonic acid (PFOS), a canonical PFCs, elevated the atherogenic risk in mice fed with HFD, which was characterized by an increased number of pro-inflammatory phenotype macrophages. We also found that macrophages exhibited a metabolic reprogramming to glycolysis, which was attributed to increased intracellular Fe^{2+} level. Mechanistic investigation revealed that PFOS directly bound to the iron-storage site on the ferritin heavy chain, subsequently weakening the iron-storage function. Notably, PFCs with acidic substituents and short chains had a higher atherogenic risk, as evidenced in the crucial indicators and observed in a population with a high triglyceride level. These findings highlight the potential atherogenic risk posed by PFCs exposure in susceptible populations consuming HFD and provide a potential intervention target.

Keywords: PFCs, macrophage phenotype, energy metabolism, FTH, atherosclerosis

Significance Statement

The pathogenesis and progression of atherosclerosis are exacerbated by the combined effect of multifaceted risk factors, underscoring the necessity for comprehensive inquiries into key factors such as dietary patterns and environmental risks. Here, we reported that perfluorinated compounds with acidic substituents and short carbon chains possess pro-atherogenic characteristics through Fe^{2+}-mediated metabolic reprogramming and macrophage phenotype transformation mechanisms. The findings shed new light on the previously unrecognized atherogenic risks related to exposure to environmental pollutants among increasing populations consuming high-fat diets, emphasizing the imperative for a comprehensive investigation into the cardiovascular disease risks and underlying mechanisms resulting from the intricate interplay of multifaceted risk factors.

Introduction

Cardiovascular disease is one of the leading causes of global morbidity and mortality (1). Atherosclerosis, conceptualized as a chronic inflammatory disease, serves as the primary precursor to the development of cardiovascular diseases (2). Early identification and intervention in atherosclerosis are pivotal in forestalling more severe cardiovascular events (3). The pathogenesis and progression of atherosclerosis are exacerbated by multifaceted risk factors, encompassing metabolic risks (e.g. elevated low-density lipoprotein cholesterol [LDL-C] levels), behavioral risks (e.g. dietary habits), and environmental risks (e.g. exposure to organic pollutants) (1, 4–6). This complexity underscores the necessity for

Competing Interest: The authors declare no competing interests.
Received: August 29, 2024. **Accepted:** May 2, 2025

comprehensive inquiries into the risks and underlying mechanisms of the important factors.

Among the risk factors contributing to atherosclerosis, dietary habits emerge as a major motivation for elevated LDL-C levels (7). In recent decades, a dietary pattern characterized by high-fat consumption has risen in popularity, primarily driven by the demands of a fast-paced lifestyle and the need for calorie-dense foods in the context of rapid socioeconomic advancements (7). Data from the latest iteration of the Dietary Guidelines for Chinese Residents indicate a marked increase in the consumption of high-fat foods, with prevalence rates reaching up to 67.9% (8). The ingestion of high-fat diets (HFDs) has been demonstrated to elevate blood cholesterol levels, which can instigate atherosclerosis through the initiation of an inflammatory cascade (9). Consequently, the HFD pattern enhances individual susceptibility to atherosclerosis. Moreover, the interplay of such dietary practices with environmental exposure may markedly aggravate the atherogenic risk.

Among the environmental risk factors, perfluorinated compounds (PFCs), which have emerged as global persistent organic pollutants, have attracted considerable public concern due to their widespread detection in human and environmental matrices and the associated potential health risks (10, 11). The general population is mainly exposed to PFCs through dietary intake, with significant sources of the PFCs in food packaging, cookware coatings, and drinking water (12, 13). Notably, a recent study has documented the detection of PFCs in over 98% of blood samples from the US population (10). The cross-sectional studies in China reported that the serum levels of PFCs, notably perfluorooctanoic acid (PFOA), in the local inhabitants were elevated by a factor of 1–3 orders of magnitude, surpassing those concentrations typically reported in the global population (14). Specifically, perfluorooctane sulfonic acid (PFOS), a representative PFCs, has been found at internal exposure concentrations reaching up to 10 μg/mL in human blood (15). Epidemiological evidence has identified PFCs as a significant environmental risk factor for atherosclerosis (16, 17). In light of the growing prevalence of HFD, the number of PFC-exposed populations who consume such diets will inevitably increase, and these individuals may be at a higher risk of atherosclerosis. This situation necessitates a comprehensive understanding of risk characteristics and underlying mechanisms of PFC-related atherosclerosis in populations with an HFD pattern, with implications for the development of targeted preventive measures to mitigate the associated risks.

Here, our data unveiled the risk, characteristics and underlying mechanisms of PFC-caused atherosclerosis in increasingly susceptible populations with an HFD pattern. We found that PFOS, a representative compound among the various PFCs, significantly exacerbated atherogenic risk in HFD-fed mice. Mechanistically, we identified that a heightened pro-inflammatory state and dysfunctional traits in arterial macrophages, regulated by the PFOS-prompted metabolic reprogramming toward glycolysis, were the key causation of PFOS-promoted atherogenic risk. We also uncovered a target of accumulated intracellular Fe^{2+} induced by the direct binding of PFOS on the iron-storage site of ferritin heavy chain (FTH) and compromised iron-storage capacity. The chelated intracellular Fe^{2+} reversed energy metabolism toward glycolysis and pro-inflammatory state in macrophages. Moreover, PFCs with acidic substituents and short chains posed a higher atherogenic risk, which was validated in populations with a higher triglyceride (TG) level. These findings underscore the atherogenic potential of PFCs exposure for the increasingly susceptible population with an HFD pattern and suggest novel intervention strategies for preventing the atherogenic risk of PFCs.

Results

PFOS promotes the atherogenic risk characterized by macrophage elevation in HFD-fed mice

To investigate the atherogenic risk of environmental dose PFOS exposure under an HFD pattern, C57BL/6J mice were fed a normal chow diet (NCD) or HFD co-administered with or without PFOS for 8 weeks (Fig. S1A). Compared with the NCD group, the HFD group exhibited a marked elevation in liver coefficient (Fig. S1B). Total cholesterol (TC) and TG levels were increased, indicating the hyperlipidemic condition of mice (Fig. S1C). Compared with that in HFD-fed control mice, the liver organ coefficient was also increased in PFOS exposure of HFD-fed mice (Fig. S1B). Levels of TC and TG were also elevated (Fig. S1C), indicating that PFOS exacerbated the hyperlipidemic condition in mice. Furthermore, the entire aorta from PFOS exposure of HFD-fed mice exhibited more prominent atherosclerotic plaque areas compared with the HFD control (Fig. 1A and B). Further aortic valve pathological structure staining showed that PFOS led to the remarkable reduction of collagen fibers in the aortic wall of HFD-fed mice (Fig. 1C and D). The aortic root from PFOS exposure of HFD-fed mice displayed a thickened aortic wall, accompanied by markedly enhanced inflammation (depicted by arrows in Fig. 1E and F).

Macrophages are the major immune cell population in atherosclerotic plaques, and the formation of macrophage foam cells in the intima is a major hallmark of atherosclerosis (18, 19). Arterial inflammation was further evaluated by the immunofluorescence of macrophages. The levels of macrophages in the aorta labeled by CD68 were significantly increased in PFOS exposure of HFD-fed mice when compared with the HFD control mice (Fig. 1G and H). Then, we detected the arterial foam cells. As shown in Fig. 1I, PFOS led to a significantly enhanced proportion of foam cells in the aortic root of HFD-fed mice (Fig. 1J). Together, these data suggest that PFOS exposure promotes the atherogenic risk of HFD-fed mice, evidenced by the apparent elevation of macrophages.

PFOS enhances the macrophages' phenotypes toward a pro-inflammatory state and abnormal function

The phenotypic characteristics and functions of macrophages in the aorta are closely related to the atherosclerotic process (20). To further define the phenotypic alteration of arterial macrophages, we gated two subsets of arterial macrophages based on the levels of cell surface markers, classical activation macrophages (CAMs), and alternative activation macrophages (AAMs; Fig. S2). Compared with the HFD-fed control mice, PFOS exposure obviously accumulated CAM but reduced AAM, manifested by both the cell proportions (Fig. 2A and B) and numbers (Fig. 2C). PFOS also promoted CAM-related *Tnf-α* and *Il-1β* expressions but suppressed AAM-related *Mrc-1*, *Fizz1*, and *Ym-1* expressions in the aortas of HFD-fed mice (Fig. 2D). Likewise, primary murine bone marrow–derived macrophage (BMDM) co-treated with PFOS and oxidized LDL (oxLDL; Fig. 2E), simulating macrophages in hyperlipidemic condition, exhibited enhanced levels of pro-inflammatory genes and decreased levels of anti-inflammatory genes (Fig. 2F). The increased protein level of iNOS, an important molecular indicator for CAM (Fig. S3), also confirmed the macrophage phenotypes toward a pro-inflammatory state promoted by PFOS.

The pro-inflammatory state of macrophages is generally linked with the increased vascular endothelial cell adhesion and uptake of oxLDL, the critical functions of macrophages in the progression of atherosclerosis (21). Following the co-culture of primary

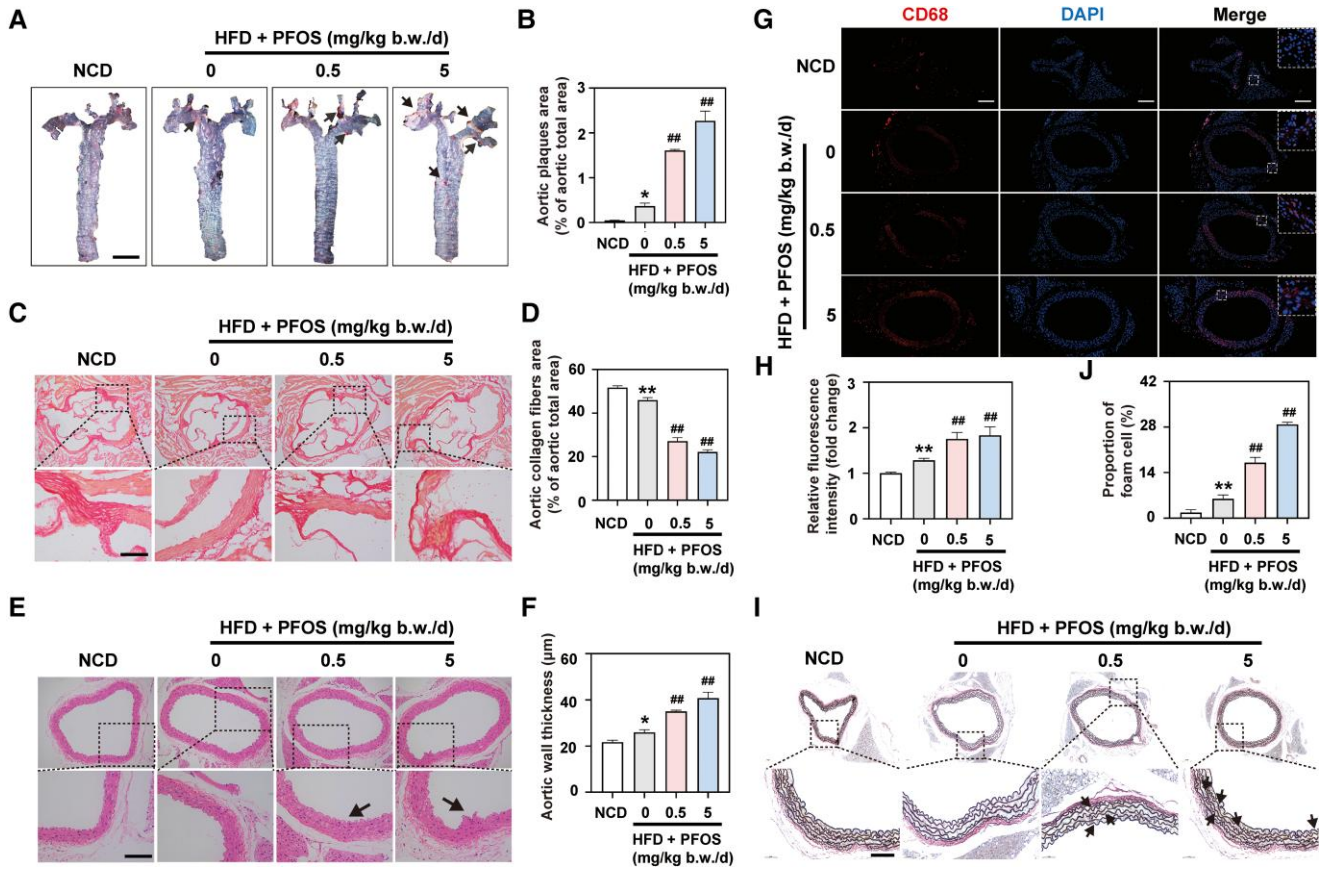

Fig. 1. Atherogenic risk in HFD-fed mice promoted by PFOS exposure. A) Representative images of ORO staining in the aorta (arrows indicate atherosclerotic plaques in the aorta) and B) the quantitative result of atherosclerotic plaque areas. Plaque areas were calculated as percentages of the total surface areas of the whole aorta. Scale bar, 3 mm. C) Representative images of VG-stained aortic and D) quantification for the aortic collagen fiber area. Scale bar, 50 μm. E) H&E staining for aortic roots and F) corresponding quantification of aortic wall thickness. The arrows indicate inflammatory infiltration of the aortic wall. Scale bar, 50 μm. G) Immunostaining for CD68 in mouse aortic roots and H) quantification of CD68-positive levels. Scale bar, 200 μm. I) Movat's pentachrome staining for cross-sections of aortic roots and (J) quantification of foam cells in plaque. The arrows indicate foam cells in the plaque. Scale bar, 50 μm. Data are presented as mean ± SD. $^{*}P < 0.05$ and $^{**}P < 0.01$ versus NCD-fed mice group, respectively. $^{\#}P < 0.05$ and $^{\#\#}P < 0.01$ versus the HFD-fed mice group, respectively.

murine macrophages and vascular endothelial cells (Fig. 2G), we found that PFOS treatment significantly increased the number of adherent macrophages to vascular endothelial cells, when compared with the oxLDL treatment alone group (Fig. 2H and I). Moreover, PFOS promoted the uptake of oxLDL by macrophages, as shown by increased oil-red O (ORO)-positive cells (Fig. 2J and K). Similar results were also observed in the co-culture of human macrophages and vascular endothelial cells (Fig. S4). These findings suggest that PFOS exposure accelerates the phenotypic transformation of pro-inflammatory macrophages and enhances the capacity of cell adhesion and oxLDL uptake.

PFOS augments the pro-inflammatory macrophages through a metabolic switch to glycolysis

A transcriptomics analysis was performed to interrogate how PFOS accelerated macrophage phenotypes toward a pro-inflammatory state under the hyperlipidemic condition. Pathways analyzed from Kyoto Encyclopedia of Genes and Genomes (KEGG) enrichment were mainly involved in the metabolism pathway (Fig. S5A), among which glycolysis in energy metabolism was the main response pathway (Fig. 3A). The reduced ATP levels in both PFOS-treated BMDM (Fig. 3B) and human-derived macrophages (Fig. S6A) also illustrated the abnormal energy metabolism of macrophages. Targeted metabolomics showed that the contents of metabolites in glycolysis were increased in the PFOS-treated group when compared with the oxLDL treatment alone group (Fig. 3C). Results from kits also confirmed the elevated contents of pyruvate and lactate (i.e. the products of glycolysis) (Figs. 3D and S6B). Moreover, PFOS enhanced the uptake ability of BMDM to glucose (Figs. 3E and S6C) and the mRNA level of *Glut1*, the glucose transporter (Fig. S5B). PFOS also up-regulated the levels of rate-limiting enzymes of glycolysis, including the protein level of hexokinase (HK; Figs. S5C, D and S6D) and mRNA levels of *Pkm2* and *Ldha* (Figs. S5E and S6E). The integrated mapping showed that glycolysis was promoted by PFOS treatment under the hyperlipidemic condition (Fig. 3F).

Glycolysis is one of the important energy metabolism pathways. In order to obtain a more comprehensive understanding of the impact of PFOS on the energy metabolism of macrophages, we further assessed the alteration of other energy metabolic pathways caused by PFOS by targeted metabolomics analysis. Our results showed the alteration of aerobic energy metabolic pathways, such as decreased oxidative phosphorylation and no significant changes in tricarboxylic acid (TCA) levels (Fig. S7A). The down-regulated levels of mitochondrial respiratory complexes I–V also confirmed the attenuated oxidative phosphorylation by PFOS in

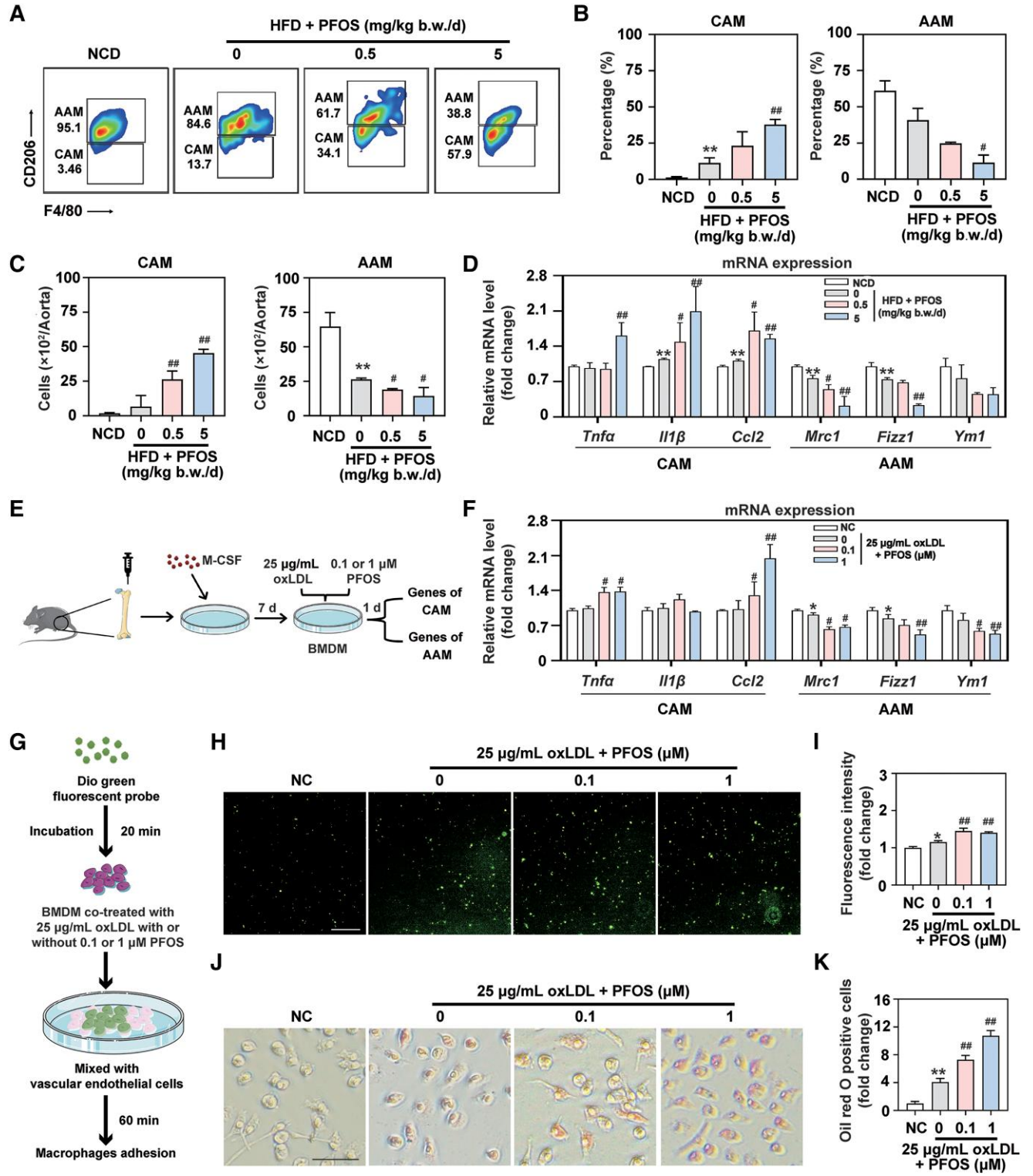

Fig. 2. Phenotypic and functional alteration of macrophages promoted by PFOS exposure under the hyperlipidemic condition. Cell percentages (A and B) and number (C) of CAMs and AAMs. D) Relative mRNA expressions of pro- or anti-inflammatory genes in the aorta. Data are presented as mean ± SD, $^{*}P < 0.05$ and $^{**}P < 0.01$ versus the NCD-fed mice group, respectively. $^{\#}P < 0.05$ and $^{\#\#}P < 0.01$ versus the HFD-fed mice group, respectively. E) Flowchart of primary murine BMDM treated by PFOS (0.1 or 1 μM) and oxLDL (25 μg/mL). F) Relative mRNA expressions of pro- or anti-inflammatory genes in the BMDM. NC was the negative control. G) Flowchart of co-culture of PFOS-treated BMDM and vascular endothelial cells. H) Representative images and I) quantitative analysis of adherent macrophages stained by the Dio fluorescent probe to vascular endothelial cells. Scale bar, 500 μm. J) Representative images and K) quantitative analysis of BMDM using ORO staining. Scale bar, 50 μm. Data are presented as mean ± SD, $^{*}P < 0.05$ and $^{**}P < 0.01$ versus the NC group, respectively. $^{\#}P < 0.05$ and $^{\#\#}P < 0.01$ versus oxLDL treatment alone group, respectively.

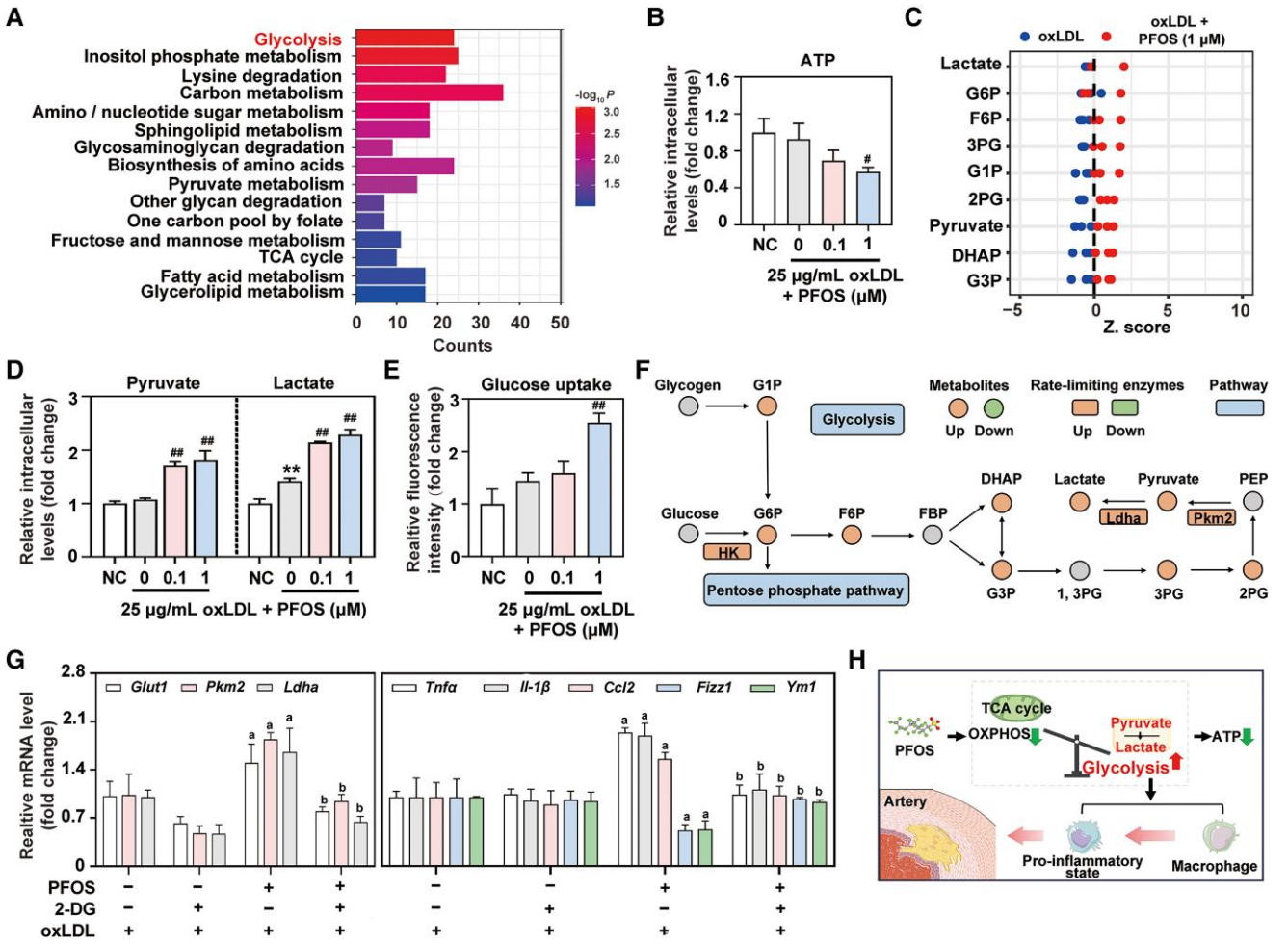

Fig. 3. Role of glycolysis in the pro-inflammatory phenotype of macrophages promoted by PFOS under the hyperlipidemic condition. A) Top 15 KEGG pathways of enrichment analysis for differentially expressed genes in BMDM co-treated with PFOS and oxLDL. B) Content of cellular ATP in BMDM. NC was the negative control. C) Different glycolytic metabolites in the oxLDL (25 μg/mL) treatment alone group, and co-treated group with PFOS and oxLDL, each dot represents a single sample. D) Contents of pyruvate and lactate in BMDM. E) Glucose uptake of BMDM. F) KEGG pathway mapping containing metabolites and rate-limiting enzymes in BMDM affected by PFOS. Data are presented as mean ± SD, $^{*}P < 0.05$ and $^{**}P < 0.01$ versus the NC group, respectively. $^{\#}P < 0.05$ and $^{\#\#}P < 0.01$ versus oxLDL treatment alone group, respectively. G) Relative mRNA expressions of genes related to glycolysis, pro-inflammatory, and anti-inflammatory upon PFOS exposure with or without 2-DG (10 μM). $^{a}P < 0.05$ versus oxLDL treatment alone group, respectively. $^{b}P < 0.05$ versus the co-treated group with PFOS and oxLDL. H) Schematic representation for a critical role of glycolysis in the regulation of phenotype transformation of macrophages promoted by PFOS under the hyperlipidemic condition.

both BMDM (Fig. S7B) and human-derived macrophages (Fig. S7C). TCA cycle–related genes, including *Ogdh*, *Mdh*, and *Cs*, were not affected by PFOS exposure in BMDM cells (Fig. S7D), but decreased in human-derived macrophages (Fig. S7E). The integrated mapping showed that oxidative phosphorylation was weakened by PFOS treatment under the hyperlipidemic condition (Fig. S7F). The data indicated that PFOS promoted the metabolic reprogramming of macrophages from aerobic energy metabolism to glycolysis.

2-Deoxy-D-glucose (2-DG), an inhibitor of glycolysis, was utilized to investigate the role of glycolysis in the pro-inflammatory macrophages promoted by PFOS (Fig. S8A). Supplementation of 2-DG effectively rescued the alteration of glycolysis-related genes promoted by PFOS (Fig. 3G). Furthermore, PFOS-increased level of iNOS was inhibited by the co-treatment of 2-DG (Fig. S8B). Likewise, mRNA levels of *Tnf-α*, *Il-1β*, and *Ccl2* related to pro-inflammatory were down-regulated by the co-treatment of 2-DG, whereas mRNA levels of *Fizz1* and *Ym-1* related to anti-inflammatory were up-regulated (Fig. 3G). Therefore, PFOS can augment the pro-inflammatory macrophages through metabolic reprogramming toward glycolysis (Fig. 3H).

PFOS enhances the glycolysis of macrophage via the mediation of elevated Fe^{2+} due to the weakened iron-storage function of FTH

Next, we intend to uncover the underlying mechanism of PFOS-promoted glycolysis in macrophages. Our previous study demonstrated that PFOS has a high affinity for ferritin (i.e. fundamental iron-storage protein in cells) (22). Ferritin is a heterodimeric complex composed of two major subunits, FTH and ferritin light chain (FTL) (23). Macrophages were identified as the primary cell type exhibiting high levels of FTH and FTL, according to the mouse cell atlas analysis (Fig. S9). Therefore, we speculated that PFOS regulated macrophages to adopt a glycolytic state by directly

interfacing with ferritin within the macrophages. To verify this hypothesis, we first assessed the binding ability between PFOS and critical sites (iron-storage site and catalytic site) of ferritin. PFOS is primarily bound to the iron-storage site of ferritin rather than to its catalytic site (Fig. 4A). Moreover, a stronger binding affinity between PFOS and FTH was observed compared with the interaction between PFOS and FTL. This observation was corroborated by molecular dynamics (MD) simulations (Fig. 4B), suggesting that the iron-storage function of FTH was disturbed by PFOS treatment. We then detected the Fe^{2+} level of macrophage, an important indicator for the iron-storage function of ferritin (24). Both immunofluorescence (Fig. 4C and D) and flow cytometry (Fig. S10A) results showed the significant elevation of Fe^{2+} content caused by PFOS treatment when compared with the oxLDL treatment alone. After the oxidation of Fe^{2+} to Fe^{3+}, Fe^{3+} was stored at the iron-storage site of ferritin (25); thus, the accumulation of Fe^{2+} suggested the weakened iron-storage function of ferritin.

To determine the role of Fe^{2+} accumulation in the regulation of macrophages to adopt a glycolytic and pro-inflammatory state, clioquinol (CQ), a Fe^{2+} chelator, was utilized. Complement of CQ markedly increased ATP content in BMDM, when compared with the PFOS and oxLDL co-treatment group (Fig. 4E). As for the alteration of glycolysis-related indicators, glucose uptake capacity (Fig. 4F), lactate level (Fig. 4G), and related gene levels (Fig. S10B) were reversed by the co-treatment with CQ. In addition, expressions of *Tnf-α*, *Il-1β*, and *Ccl2* related to pro-inflammatory were increased by the co-treatment of CQ, whereas levels of *Fizz1* and *Ym-1* related to anti-inflammatory were decreased (Fig. 4H). Consequently, the Fe^{2+} augmentation assumes a pivotal function in the metabolic and phenotypic alteration of macrophages stimulated by PFOS.

We further explored the binding of PFOS with FTH and uncovered its mechanism for undermining the iron-storage function of FTH. A predominant alteration of α-helix structure (i.e. the protein secondary structure in which the iron-storage site is mainly located) in the complex of PFOS and FTH was predicted (Fig. 4I). The data from interaction energy of PFOS and key amino acid residues of FTH revealed that His-65 and Glu-140 (both located in the α-helix) emerged as the pivotal binding amino acids (Fig. 4J), thus causing the secondary structure alteration of FTH. In the conformational diagram of Fig. 4K, the strong hydrogen bond interaction between PFOS and His-65 or Glu-140 was 1.87 and 2.18 Å, respectively, indicating that PFOS formed stable noncovalent interactions with FTH by penetrating into its iron-storage site. Moreover, the energy decomposition of the complex system (i.e. PFOS and ferritin) found that the system difference between PFOS binding with FTH and FTL was mainly caused by electrostatic energy (ΔG(ele)) (Fig. S11), related to hydrogen bond strength, confirming the specific interaction of PFOS and FTH was significantly influenced by hydrogen bonding. Therefore, the binding of Fe^{3+} to the iron-storage site of FTH was hindered, resulting in Fe^{2+} accumulation and a reduced iron-storage function of ferritin.

We used Fourier infrared spectroscopy and circular dichroism (CD) spectroscopy to further confirm the binding and structure alteration of FTH with PFOS. Obviously, PFOS altered the amide I band (1,600–1,700 cm^{-1}, depicted by the dashed box) absorption peak of FTH protein (Fig. 4L), indicating secondary structure alteration of FTH. CD analysis further revealed a marked change in the proportion of α-helical structures of FTH (Fig. 4M), confirming the binding of PFOS to the iron-storage site of FTH, thereby weakening the iron-storage function. Together, PFOS blocked the iron-storage site of FTH (His-65 and Glu-140) and led to the accumulation of Fe^{2+} in macrophages. As a consequence, this process drives energy metabolism toward glycolysis and pro-inflammatory state (Fig. 4N).

PFCs with acidic substituents and short carbon chains have a higher atherogenic risk under hyperlipidemic condition

To obtain a comprehensive understanding of the potential atherogenic risks of PFCs, 24 PFCs, which have been widely detected in the environment (26, 27), were recruited in the current study. As depicted in the preliminary screening flowchart (Fig. 5A), initial analysis yielded 15 descriptors for the 24 PFCs and their binding affinities with the iron-storage site on FTH (Fig. S12A and Table S1). Subsequently, the XGBoost, a robust machine learning model, was employed to train a predictive model that was capable of estimating the potential perturbations of PFCs on the iron-storage function of FTH (Fig. S13). The result indicated that substituent type (accounting for 88.76%) and carbon chain length (contributing 8.63%) were pivotal factors influencing the binding affinity of PFCs to the iron-storage site of FTH (Figs. 5B and S12B). Therefore, we next focused on the influence of two classes of structural descriptors, substituent type and carbon chain length, on binding affinity. Further comparison of binding affinity between PFCs with different substituents and FTH showed that PFCs with acidic substituents (–SO_3H [−7.23 ± 0.14 kcal/mol], –COOH [−5.53 ± 0.04 kcal/mol]) exhibited a higher binding ability to FTH, under the same carbon chain length (C:6 and C:8; Fig. 5C). The linear correlation between the carbon chain lengths of PFCs and their binding affinities to FTH, under the same substituent type (–COOH substituent or –OH substituent), indicates that PFCs with short carbon chains had a higher binding affinity for FTH (Fig. 5D). Together, machine learning model prediction suggested that PFCs with higher binding affinity with FTH may have greater effects on the Fe^{2+}, glycolysis, and pro-inflammatory levels of macrophages.

PFCs with different substituent types and carbon chain lengths (Tables S2 and S3) were thus selected for the subsequent evaluation of cell experiments, including Fe^{2+}, glycolytic genes, and pro-inflammatory gene levels. As illustrated in Fig. 5E and Table S4, treatment with PFCs containing acidic substituents and PFCs with shorter carbon chains induced a significant increase in intracellular Fe^{2+} levels in macrophages, compared with oxLDL treatment alone. Specifically, PFCs bearing a –SO_3H group exhibited the most significant enhancement of intracellular Fe^{2+} level, followed by PFCs with a –COOH group. In terms of carbon chain length, PFCs with a carbon chain length of C:4 were the most potent, followed by those with a C:8 chain length. Consistently, PFCs with these structural features also exhibited a greater propensity to enhance the expression of genes linked to glycolysis (Fig. S14A and B), and a more pronounced capability to promote macrophages toward a pro-inflammatory state (Fig. S14C and D).

We subsequently collected data from all critical indicators to comprehensively assess the potential atherogenic risk associated with PFC exposure. Heat map cluster analysis (Fig. 5F and G) showed that affinity and anti-inflammatory genes (*Fizz1* and *Mrc-1*) formed one cluster, while Fe^{2+}, glycolytic genes (*Glut1*, *Pkm2*, and *Ldha*) and pro-inflammatory genes (*Tnf-α* and *Ccl2*) constituted another cluster. A mixed-effects model was employed to analyze the two clusters separately. PFCs with a –SO_3H substituent illustrated the most pronounced effects on enhancing binding affinity to FTH, increasing Fe^{2+} levels, and up-regulating both glycolytic and pro-inflammatory gene expressions, followed by PFCs with a –COOH substituent, under the same carbon chain length (Fig. 5H). In terms of carbon chain length, PFCs with a C:4 chain

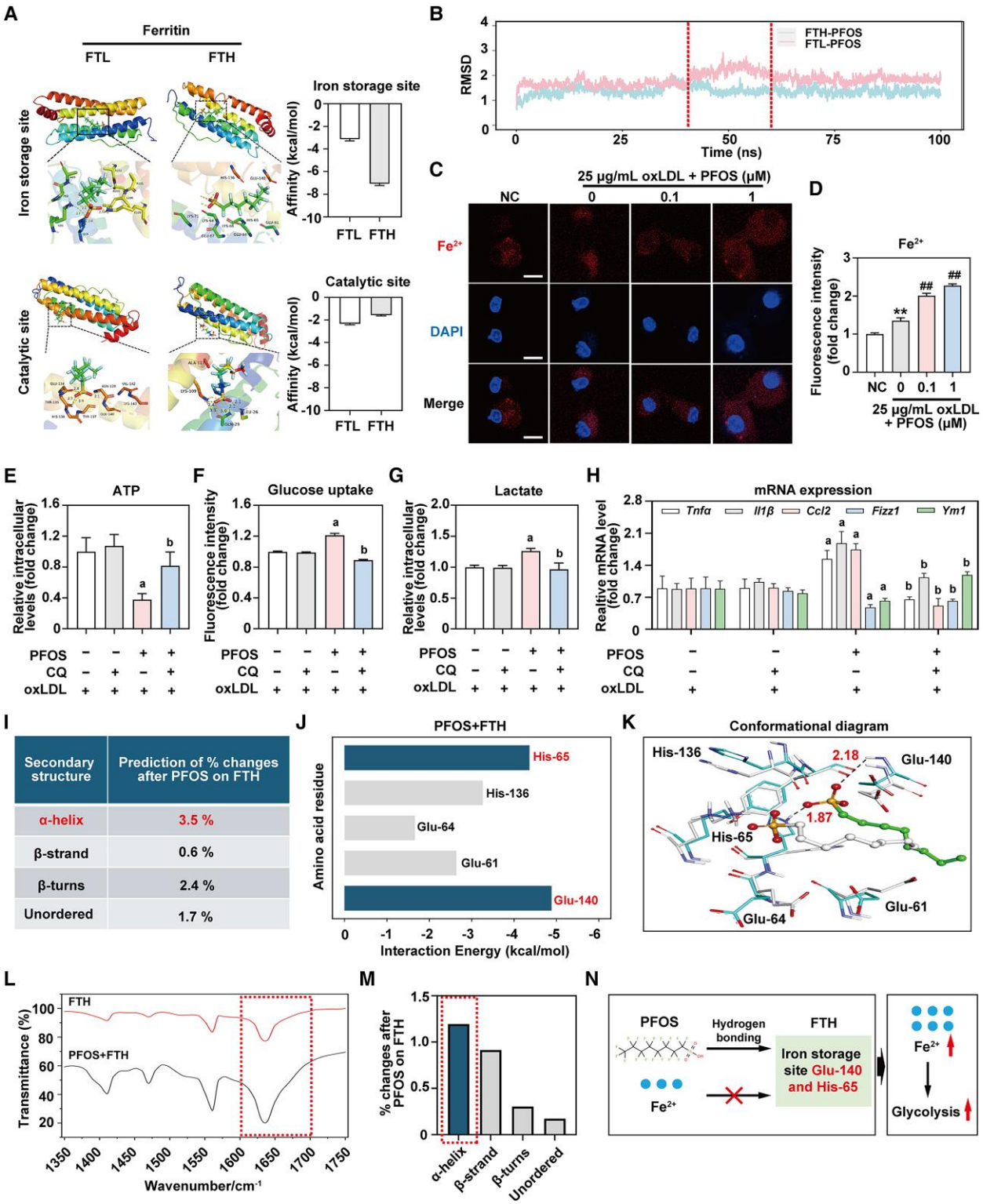

Fig. 4. Regulation of iron-storage function of FTH in glycolytic and pro-inflammatory phenotype macrophages promoted by PFOS under the hyperlipidemic condition. A) Molecular docking. PFOS binds to the iron-storage site and catalytic site of FTH or FTL, two major subunits of ferritin. B) Calculated values of RMSD for PFOS and FTH from MD simulations. C) Representative fluorescence image of the intracellular Fe^{2+} in BMDM and D) corresponding quantification. Scale bar, 10 μm. NC was the negative control. $^{**}P < 0.01$ versus NC group, $^{\#\#}P < 0.01$ versus oxLDL treatment alone group. BMDM were cotreated with PFOS and or without CQ (25 μM), Fe^{2+} chelator, under the conditions of oxLDL treatment. E) Content of cellular ATP in BMDM. Level of (F) glucose uptake and (G) lactate in BMDM. H) Relative mRNA expressions of pro-inflammatory and anti-inflammatory genes. $^{a}P < 0.05$ versus the oxLDL treatment alone group, $^{b}P < 0.05$ versus the co-treated group with PFOS and oxLDL, respectively. I) Predicted change in percentage of secondary structure of FTH after biological coupling of PFOS to FTH. J) The interaction energy of PFOS binds to the key amino acid residues of FTH. K) Conformational diagram for the complex of PFOS and FTH from MD simulations. L) Fourier infrared spectroscopy analysis of FTH bioconjugated with PFOS. The dashed box region indicates the amide I band of FTH. M) Circular dichroism analysis of FTH bioconjugated with PFOS. N) Schematic representation for regulation of iron-storage function of FTH in glycolytic and pro-inflammatory phenotype macrophages disrupted by PFOS under the hyperlipidemic condition.

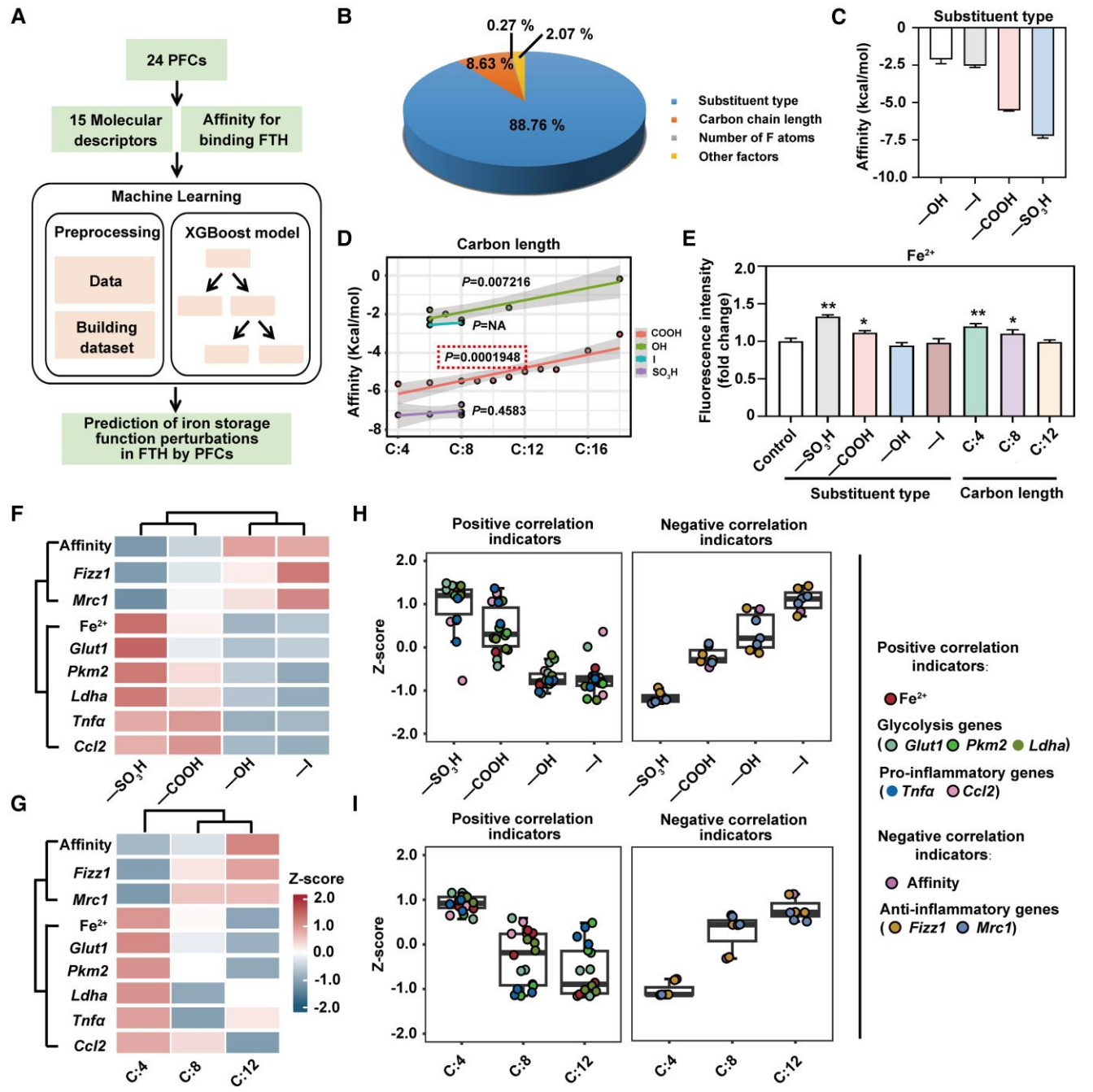

Fig. 5. Higher atherogenic risk is caused by PFCs with acidic substituent type and short carbon chain under hyperlipidemic conditions. A) Flowchart for predicting the potential perturbation of PFCs on the iron-storage function of FTH using an XGBoost model. B) Key factors for binding affinity between 24 PFCs and iron-storage site of FTH. C) Comparison of binding affinity of PFCs with different substituent types under the same carbon chain length. D) Linear correlation analysis between carbon chain length and binding affinity of PFCs and FTH under the same substituent type. (E) Intracellular Fe^{2+} content of BMDM after typical PFCs with different substituent types and carbon chain lengths exposure. Data are presented as mean ± SD, $^{*}P < 0.05$ and $^{**}P < 0.01$ versus the control group (oxLDL treatment alone group). Heat map cluster analysis for typical PFCs with (F) different substituent types and (G) carbon chain lengths and the key indicators, which include binding affinity with FTH iron-storage sites, anti-inflammatory genes, Fe^{2+}, glycolysis genes, and anti-inflammatory genes. Mixed-effects analysis for typical PFCs with (H) different substituent types and (I) carbon chain lengths and key indicators, which include binding affinity with FTH iron-storage sites, anti-inflammatory genes, Fe^{2+}, glycolysis genes, and anti-inflammatory genes.

were most potent in enhancing binding affinity to FTH, increasing Fe^{2+} levels, and up-regulating glycolytic and pro-inflammatory gene expressions, followed by C:8 and C:12 chain lengths, under the same substituent type (Fig. 5I). Collectively, our findings imply that PFCs with acidic substituents (–SO_3H and –COOH) and short carbon chains pose a higher atherogenic risk under hyperlipidemic conditions, while PFCs with long carbon chains and nonacidic substituents may be less risky.

PFCs with acidic substituents and short carbon chains have a stronger association with atherogenic indices in populations with higher TG levels

We conducted a panel study to further corroborate the potential atherogenic risk associated with exposure to PFCs within an HFD pattern. Based on the baseline survey in the summer, we divided the participants into low TG group (T1), middle TG group (T2),

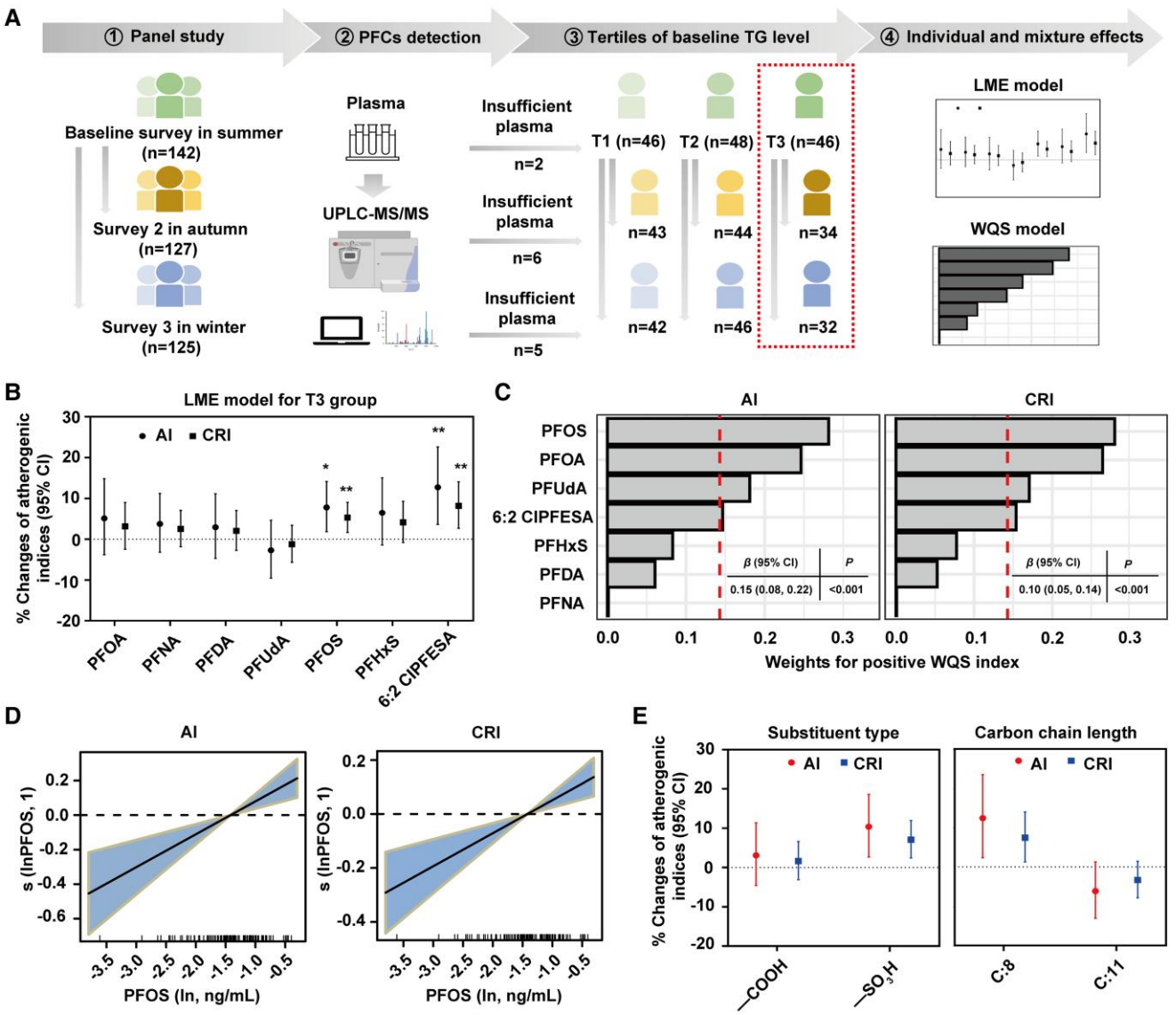

Fig. 6. Association between PFC exposure and atherogenic indices in populations with higher TG levels. A) The panel study design and workflow summary. B) Associations of individual PFCs with AI and CRI for T3 group by LME model. *P-FDR < 0.05. C) Joint effects of PFCs mixture on AI and CRI based on positive WQS regression model. D) Exposure–response relationships of PFOS with AI and CRI fitted by GAMs. E) Effects of 4 PFCs with different substituent types and carbon chain lengths on AI and CRI using multiple PFC LME models. Models were adjusted for age, gender, BMI, parental education level, passive smoking status, extra-school activity, season, and dietary variables, including the intake frequency of meat, seafood, packaged food, vegetable, and fruit.

and high TG group (T3) according to the tertiles of TG level (Fig. 6A). Characteristics of baseline participants in different groups were shown in Table S5. No significant differences were observed in seven PFCs with a detection rate >80% between the different TG groups. However, individuals in the T3 group had a higher atherosclerosis index (AI) and Castelli's risk index (CRI) compared with those in the T1 and T2 groups.

To assess the relationship between single PFCs with atherogenic indices (AI and CRI), a linear mixed effect (LME) model and a weighted quantile sum (WQS) regression model were applied. In the LME model for the overall participants, after adjusting for potential confounding variables, no significant associations were found between individual PFCs and either AI or CRI (Fig. S15). Nevertheless, in the LME model for the T3 group, each doubling of PFOS was associated with increases in AI and CRI increments of 7.82% (95% CI 1.86–14.13%) and 5.31% (95% CI 1.67–9.08%), respectively (Fig. 6B). Similarly, a 1-fold increase in 6:2 chlorinated polyfluorinated ether sulfonate (6:2 Cl-PFESA) was associated with increments in AI and CRI of 12.73% (95% CI 3.64–22.63%) and 8.22% (95% CI 2.68–14.06%), respectively. These findings indicated that PFOS and 6:2 Cl-PFESA were associated with higher AI and CRI levels in T3 group. In the WQS model, we found significant positive associations between PFCs and both AI (β [95% CI]: 0.15 [0.08–0.22]; $P < 0.001$; Fig. 6C) and CRI (β [95% CI]: 0.10 [0.05–0.14]; $P < 0.001$; Fig. 6C). PFOS, PFOA, perfluoroundecanoic acid (PFUDA) and 6:2 Cl-PFESA were identified as the main contributors, with their weights over equal weighting. Among them, PFOS contributes the most, validating its selection as a representative substance. Moreover, PFOSs were linearly positively associated with AI and CRI ($P < 0.05$; Fig. 6D), suggesting that higher PFOS concentrations increase the atherogenic risk profile in individuals with higher TG levels.

We further investigated the relationships between the identified four PFCs by WQS models and atherogenic indices, focusing

on substituent types and carbon chain lengths (Table S6). After adjusting for other PFCs, the results of multiple PFC LME models showed that PFCs with $–SO_3H$ had a more significant association with AI and CRI than PFCs with –COOH (Fig. 6E). For carbon chain length, PFCs with C:8 had a more significant association with AI and CRI than PFCs with C:11 (Fig. 6E). Together, PFCs with $–SO_3H$ substituent groups and shorter carbon chain lengths are more strongly linked to atherogenic risk among individuals with high TG levels.

Discussion

The interplay of environmental factors (i.e. widely exposed PFCs) and behavioral factors (i.e. popular HFD) may markedly aggravate the atherogenic risk, which highlights the necessity for a comprehensive inquiry into complex risk factors to investigate underlying mechanisms and uncover strategies for effective intervention. Here, we showed that the environmental dose of typical PFC (PFOS)-exposed HFD-fed mice exhibited a higher atherogenic risk, characterized by the enhanced macrophage phenotypes toward a pro-inflammatory state and abnormal function. We demonstrated that a metabolic switch to glycolysis in macrophages promoted its phenotypic transformation. Furthermore, we identified the intracellular accumulation of Fe^{2+} as a critical regulator for the aforementioned metabolic reprogramming, which was supported by the reversal of Fe^{2+} chelation. The elevated intracellular level of Fe^{2+} was induced by PFOS through direct binding to the iron-storage site on FTH, specifically His-65 and Glu-140 residues, thereby compromising its iron-storage capacity. Finally, a comprehensive risk assessment using the above crucial indicators proved that PFCs with acidic substituents and short chains had a higher atherogenic risk, as also evidenced in data from a population with a high TG level. A schematic summarization of these results is presented in Fig. S16. This study highlights the increased atherogenic risk of PFC exposure in the population consuming an HFD, suggests an intervention strategy of Fe^{2+} chelator to mitigate this atherogenic risk, and informs the choice of safer PFCs in the production and application.

People's unhealthy eating habits and environmental risk factors continue to pose significant challenges to both life and health. In the current investigation, it was observed that PFOS, a well-known environmental pollutant, induced a higher burden of aortic plaques in mice fed with HFD. These plaques exhibited characteristics of thin fibrous caps, reduced smooth muscle cells and collagen content, extensive infiltration of macrophages, and the formation of foam cells. Moreover, there was an increase in lipid deposition within the aortic intima and a thinning of elastic fibers, further exacerbating plaque instability (28, 29). Notably, the rupture of unstable atherosclerotic plaques can lead to detrimental cardiovascular events such as heart attacks, strokes, and sudden cardiac death, which are the primary causes of morbidity and mortality associated with cardiovascular diseases (30). The HFD is considered an important factor contributing to elevated TG levels (31–33). Moreover, participants in the T3 group exhibited a higher body mass index (BMI) and demonstrated a greater frequency of consumption of packaged foods and seafood compared with those in the T1 and T2 groups. Packaged food has been reported to cause an increase in BMI (7), and epidemiological evidence shows that blood TG level is significantly affected by body weight status and body fat distribution (34). These suggest that the participants with high TG levels may, to a certain extent, be indicative of a demographic that follows a high-fat dietary pattern. Similarly, a dose–response relationship between PFOS and AI (or CRI) was observed in individuals with high TG levels. These findings provide a more profound understanding of the intricate interplay between an HFD and environmental risk factors in exacerbating the risk of atherosclerosis.

The pathophysiology of vascular diseases hinges critically on inflammation. Atherosclerosis is a prototypical chronic inflammatory disease (35). Activated immune cells with an intricate imbalance between pro-inflammatory and anti-inflammatory processes are pivotal in orchestrating the persistent inflammation that underlies the development and progression of atherosclerotic plaques within the vessel walls (36). In this study, we observed that PFOS exposure facilitated increased infiltration of macrophages into the aorta and promoted their polarization toward a pro-inflammatory phenotype in HFD mice. The innate immune response constitutes an early activating force in the onset of atherosclerosis, preceding the engagement of adaptive immunity (35). Within the framework of innate immune response, macrophages emerge as key players in the initiation and progression of atherosclerosis. These cells avidly internalize oxLDL through scavenger receptors, leading to the formation of foam cells, which are considered a definitive characteristic of atherosclerotic lesions (37). The retention of cholesterol-laden macrophages within the arterial wall serves to exacerbate the progression of atherosclerosis (38). HFD is recognized as a risk factor for atherosclerosis. A previous study has highlighted the increased macrophage accumulation and the triggering of inflammatory responses in obese mice induced by HFD (39). HFD markedly increased the proportion of macrophages among aortic immune cells, from 16.16 to 45.49%, showcasing significant heterogeneity (40, 41). Our findings align with previous reports, revealing that HFD markedly enhances the proportion of macrophages exhibiting a pro-inflammatory phenotype while concurrently reducing the presence of the anti-inflammatory phenotype. Macrophages polarized in this manner secrete a battery of inflammatory mediators that intensify the inflammatory response, which is further exacerbated by PFOS exposure. This compound seems to act as a catalyst in the exacerbated cascade of events leading to the advancement of atherosclerosis.

Metabolic reprogramming has emerged as a pivotal characteristic of the innate immune response, serving not only as an energy currency but also as a regulator of macrophage phenotype and function (42). Among these metabolic alterations, the induction of glycolysis is widely recognized as a core feature of inflammatory macrophages. In our study, comprehensive transcriptomic, metabolomic, and glycolysis inhibition intervention analyses consistently revealed that PFOS-induced macrophage metabolism favors glycolysis, thereby driving a pro-inflammatory phenotype under hyperlipidemic condition. Glycolysis drives the inflammatory macrophage response through diverse mechanisms. The glycolytic enzyme PKM2 not only triggers the expression of pro-IL-1β but also facilitates inflammasome activation (43). Elevated glycolysis in individuals with coronary artery disease can lead to the production of mitochondrial reactive oxygen species, resulting in PKM2 assembly and subsequent nuclear translocation. Upon nuclear localization, PKM2 phosphorylates and activates the signal transducer and activator of transcription 3, thereby enhancing the synthesis of the inflammatory cytokines IL-1β and IL-6 (44). In addition, glyceraldehyde 3-phosphate dehydrogenase, another key enzyme in the glycolytic pathway, can regulate TNF-α secretion in a specific manner (45). Lipid metabolism constitutes a pivotal metabolic pathway within macrophages (46), with crosstalk observed between lipid and energy metabolism. During the incipient phases of atherosclerosis, macrophages engulf oxLDL, resulting in lipid accumulation and potential

dysregulation of lipid metabolic processes (47). Our prior investigations have elucidated the complex interplay of environmental pollutants disrupting macrophage cholesterol metabolism during foam cell formation (48, 49). Interestingly, KEGG enrichment analysis in this study revealed that lipid metabolic pathways were indeed enriched, albeit trailing behind the enrichment of energy metabolic pathways in terms of magnitude. The lipid metabolism in macrophages not only governs phagocytic activities but also supplies essential energy substrates (50). It is imperative to recognize that glucose, rather than lipids, serves as the predominant energy source for aortic macrophages (51). Moreover, cholesterol biosynthesis and trafficking within macrophages are intimately associated with energy metabolic functions (52, 53). Hence, energy metabolism emerges as a critical determinant of macrophage functionality.

The presence or absence of PFOS in the aorta could imply direct or indirect influences of PFOS on the development of atherosclerosis. In our study, the concentration of PFOS in the aorta reached 0.57 and 2.49 μg/mg in 0.5 and 5 mg/kg b.w./day groups, respectively (Table S7). In vitro experiments also demonstrated that PFOS can be taken up by macrophages (Table S8), suggesting that PFOS can directly infiltrate the aortic macrophages. Furthermore, a previous study has identified ferritin as a potential target of PFOS through matrix thermal shift analysis (22). Our findings reveal that PFOS preferentially binds to iron-storage sites His-65 and Glu-140 on the α-helix of FTH, impeding Fe^{3+} binding and thereby reducing the iron-storage capacity. Although other iron-storage compartments exist, PFOS uniquely establishes robust hydrogen bonds with two pivotal amino acid residues, His-65 and Glu-140. These interactions predominantly contribute to the energetic considerations. Interestingly, the level of FTH was increased in mouse aortae and BMDM (Fig. S17), which logically leads to a decrease of Fe^{2+} level by its function as an iron-storage agent. Contrary to this expectation, our findings revealed that the intracellular concentration of Fe^{2+} had also increased. We infer that the elevated Fe^{2+} levels result from PFOS directly targeting the iron-storage site of FTH, thereby compromising its iron sequestration capacity, independent of the abundance of FTH protein. Moreover, the elevated Fe^{2+} level has been reported to increase glycolysis (54). It could directly bind to pyruvate dehydrogenase kinase and up-regulate the expression of Glut1 (55). Moreover, Fe^{2+} participates in energy metabolism via the electron transport chain. Consistently, the chelation of Fe^{2+} mitigated glycolytic levels and attenuated the propensity for macrophages to adopt a pro-inflammatory phenotype, suggesting that Fe^{2+} chelation could emerge as a pivotal strategy against atherosclerosis.

We also propose that PFCs with acidic substituents and short carbon chains have a higher risk for atherogenesis, which are consistent with a previous report on PFC-induced hepatotoxicity (56). Consistent with the above findings, the results from subjects with high TG levels further confirmed that PFCs identified by the WQS models with $–SO_3H$ and shorter carbon chains present a higher atherogenic potential. Unfortunately, PFCs with –OH and –I substituent types were not detected in the present study. Nevertheless, the results provide some theoretical guidance for the future development of safer PFCs. Future studies will incorporate comprehensive dietary questionnaires and a larger sample to better understand the relationship between PFC exposure and atherogenic risk, considering different substituent types and carbon chains. In addition, the pivotal role of substituent type and carbon chain length in determining the binding affinity strength of ferritin suggests several potential mechanisms (57, 58): (i) the high electronegativity of acidic substituents fosters closer molecular interactions, intensifying their binding affinities with other molecules; (ii) enhanced hydrogen bond formation facilitated by oxygen atoms in acidic substituents promotes their stability in molecular associations; (iii) shorter carbon chains reduce molecular contact areas, thereby increasing their strength of intermolecular interactions; (iv) increased flexibility in molecules with shorter chains allows for a better alignment with coordination geometries upon binding; and (v) reduced conformational degrees of freedom in short-chain molecules mitigate their entropy loss during binding. These factors highlight the complexity of PFCs with short carbon chain and acidic substituent affecting the iron-storage capacity of FTH, which in turn leads to Fe^{2+} elevation, macrophage energy metabolism and phenotypic transition, and increased risk of atherosclerosis.

Conclusion

Our findings demonstrated that PFCs with acidic substituents and short carbon chains caused a higher atherogenic risk among populations with an HFD pattern. Notably, PFCs impaired the iron-storage function of FTH through their direct binding to the iron-storage site, causing intracellular accumulation of Fe^{2+}. Chelation of Fe^{2+} in macrophages reversed metabolic reprogramming toward glycolysis and its resulting pro-inflammatory state. These results provide insights into the mechanism of the atherogenic risk related to PFC exposure in HFD populations, which may guide the selection of safer forms of PFCs in production and application.

Materials and methods

Animal and cell experiment section

Reagents

PFOS (CAS 1763-23-1, 99%), PFOA (CAS 335-67-1, 99%), perfluorooctyl iodide (PFOI, CAS 507-63-1, 99%), 3,3,4,4,5,5,6,6,7,7,8,8,8-tridecafluoro-1-octanol (6:2 FTOH, CAS 64773-44-0, 99%), perfluorododecanoic acid (PFDoA, CAS 307-55-1, 99%), and heptafluorobutyric acid (PFBA, CAS 375-22-4, 99%) were purchased from Dr Ehrenstorfer (Germany). The stock solutions of all chemicals were prepared in dimethyl sulfoxide (DMSO, Solarbio, China) for in vitro study (1 mmol/L), among which PFOS was also dissolved in Tween 80 (Solarbio) for in vivo study (25 mg/mL), and then stored at 4 °C in the dark until usage. The working solutions were freshly prepared by gradient dilution of the stock solution with 0.9% sterile saline or cell culture medium for in vivo or in vitro experiments, respectively. The oxLDL was purchased from Yeasen Biotechnology (Yeasen, China). The working solutions of oxLDL (1, 5, 10, 25, and 50 μg/mL) were made by gradient dilution of the stock solution in DMSO (2 mg/mL) using a cell culture medium. The concentration of DMSO in the working solution was no more than 0.1% (v/v).

Animals and exposure strategy

Six-week-old C57BL/6 mice (18.9 ± 2.0 g) were obtained from Vital River Laboratory (Beijing Vital River Laboratory Animal Technology Co.). During the study, all the mice were allowed free access to food under constant conditions of a strict 12 h/12 h light/dark cycle at temperature (22–24 °C) and humidity (50–55%). The animal study was approved by the Committee of the Ethics Animal Experiments of Qingdao University, and the experiment was performed under the institutional guidelines for ethical animal usage.

After 1 week of acclimatization, the mice were randomly divided into four groups ($n = 12$), including the NCD group (regular diet and saline), HFD group (HFD and saline), and HFD + PFOS group (HFD and 0.5, 5 mg/kg b.w./day PFOS). Given that the reported occupational exposure level of PFOS was 0.5 mg/kg/day, the low dose of PFOS exposure in this study was considered to be an environmentally relevant dose (59). A high dose was also selected to yield a broad spectrum of toxic effects under hierarchical doses. The ingredients of the two diets are listed in Table S9. The mice were exposed to PFOS by intragastric administration once a day for 8 weeks and weighed every 2 days. A schematic of the exposure is shown in Fig. S1.

After the termination of exposure, the mice were sacrificed with CO_2 asphyxiation to collect serum and aortic samples. The serum was stored at −80 °C for lipid assays. The fresh aortic tissues were dissociated into single-cell suspensions for flow cytometry and fixed with 4% paraformaldehyde for histopathological examination. In addition, the remaining aortas were stored at −80 °C for quantitative real-time PCR (RT-qPCR) analysis.

ORO staining assay

After removing the residual fixative on the surface and attached connective tissue, the extended axis of the fixed entire aorta was dissected under stereomicroscopy (Olympus IX71, Japan). The treated aorta was incubated with ORO solution (Solarbio) for 30 min, and then the floating color was removed using phosphate-buffered saline (PBS) and 75% ethanol until it was colorless. Finally, the area of the aortic tiled intima and the area of each plaque were measured using ImageJ software (version 1.8.0). Plaque proportion = total plaque area/aortic tiled intima area × 100%.

The bone BMDM was treated with PFOS and/or oxLDL for 24 h. The groups were divided into control, oxLDL (25 μg/mL), and oxLDL + PFOS (0.1 and 1 μM) groups. Then, the cells were washed twice with 0.5 mL PBS and were fixed with ORO fixative (Solarbio) at room temperature for 20 min. After being washed with 60% isopropanol for 5 min, the cells were stained with fresh ORO staining solution for 30 min at room temperature. Excess dye in the cells was washed out with distilled water, and the cells were observed using a microscope (Olympus IX71).

Histological examination

The fresh aortic tissues from different groups were gently extracted, washed with PBS, and immediately immobilized in 4% paraformaldehyde for 24 h. For Van Gieson (VG), hematoxylin–eosin (H&E) and Movat's pentachrome staining, 4% paraformaldehyde-fixed aorta tissue samples were submitted to a sample pretreatment series, including gradient dehydration, paraffin embedding, sectioning (4 μm), staining with H&E (Servicebio, China), VG (Servicebio), or Movat's pentachrome staining (Servicebio). For immunofluorescent staining, the fixed aorta tissue samples were submitted to gradient dehydration, optimal cutting temperature compound embedding, sectioning (8 μm), antigen repairing and blocking with 3% BSA (Servicebio). The samples were then incubated with primary antibodies containing anti-CD68 (1:200; ABclonal Technology, China) and anti-FTH (1:200; ABclonal Technology) for 12 h at 4 °C, followed by incubated with the corresponding fluorescently-conjugated secondary antibody for 50 min. Pathological sections of H&E, Movat, and immunofluorescent staining were scanned and photographed using an imaging system (3DHISTECH; Pannoramic MIDI, Hungary), and then analyzed with ImageJ software (version 1.8.0).

Flow cytometry

The single-cell suspension of the aorta was obtained through mechanical and enzymatic dissociation. Enzyme digestive solution was first prepared by mixing the 4 U/mL (Liberase Thermolysin Medium), 120 U/mL DNase I, and 60 U/mL hyaluronidase (Sigma-Aldrich, United States). The fresh wild mouse aorta (length of ∼11 mm) was cut into around 1 mm^3 pieces and incubated in 1 mL mixed enzyme digestive solution at 37 °C for 1 h. After being transferred into a 2-mL centrifuge tube, the digested cell suspension was terminated with an equal volume of cell buffer (PBS supplemented with 2% fetal bovine serum), followed by filtered into a new 2 mL centrifuge tube with a 40-μm filter (Biosharp Life Sciences, China).

Following the lysis of red blood cells (RBCs) with Pharm RBC lysis buffer (Servicebio), centrifugation (400 × *g*, 10 min, 4 °C), and re-suspended, single-cell suspensions were obtained. After counting by the RWD-C100-SE automatic cell counter (RWD Life Science Co., Ltd, China), around 5×10^6 cells per sample were re-suspended in 50 μL of cell buffer and incubated with corresponding fluorescent-labeled antibodies from Biolegend (United States; APC/CY7-CD45, FITC-CD11b, PE7-F4/80, Super-Bright 436-CD80, APC-CD31, and PerCP-eFluor710-CD206) for 30 min at 4 °C. After washing the residual antibodies, cells were re-suspended with 500 μL of cell buffer and detected using a flow cytometer (Beckman CytoFLEX, United States).

RT-qPCR analysis

The total RNA samples were extracted from the aortic tissue and BMDM using the Trizol reagent (Yeasen Biotechnology), according to the protocol described previously (60). Reverse transcription of RNA into cDNA using SPARK script II RT Plus Kit (Yeasen Biotechnology). Subsequently, RT-qPCR was performed with SYBR Green (Yeasen Biotechnology) on a QuantStudio7 real-time PCR system (Thermo, United States). The target genes (Sangon Biotech, China) included pro-inflammatory macrophage biomarkers (*Tnf-α*, *Il-1β*, and *Ccl2*), anti-inflammatory macrophage biomarkers (*Mrc-1*, *Fizz1*, and *Ym-1*), glycolysis biomarkers (*Glut1*, *Ldha*, and *Pkm2*), and TCA biomarkers (*Cs*, *Ogdh*, and *Mdh*). The housekeeping gene was β-actin (Sangon Biotech). All the primer sequences are listed in Table S10.

Isolation of BMDM and cell culture

The BMDM was isolated and cultured using standard protocols (61). The skin-stripped hind legs were soaked in 75% alcohol for 20 min on ice. The mouse bone marrow was flushed out with a preconfigured culture medium, containing Dulbecco's modified eagle medium (Meilunbio, China), macrophage colony-stimulating factor (Meilunbio), and 10% fetal bovine serum (Gibco, United States) on an ultra-clean table. After fully dispersed and filtered through a 70-μm cell filter (Biosharp Life Sciences), the cells were cultured in an incubator (Thermo) at 5% CO_2 and 37 °C. At the end of 7 days, BMDM was identified by flow cytometry (Beckman CytoFLEX). The human umbilical vein endothelial cells (HUVECs) were obtained from Shanghai Institute of Biochemistry and Cell Biology, Chinese Academy of Sciences. Cell lines were cultured in F12K medium (Meilunbio) with 10% fetal bovine serum and 1% penicillin/streptomycin in a humidified atmosphere of 5% CO_2 at 37 °C.

Western blot

The BMDM samples were lysed with the RIPA solution (Meilunbio) containing 1% protease inhibitor (Meilunbio). After cryogenic

centrifugation at 13,000 × *g* for 15 min, the protein samples in supernatants were collected and determined by a BCA kit (Beyotime, China). Proteins were isolated from prepared protein samples using sodium dodecyl sulfate–polyacrylamide gel (Epizyme, China) and electrophoresed on polyvinylidene fluoride membranes (Sigma-Aldrich), which were subsequently subjected to immunoblotting. The primary antibodies included anti-iNOS (1:1,000; ABclonal Technology), anti-HK (1:1,000; ABclonal Technology), anti-FTH (1:1,000; ABclonal Technology), anti-OXPHOS (1:1,000; Abcam, United States), anti-β-actin (1:100,000; ABclonal Technology). Subsequently, the corresponding secondary horseradish antibodies (1:10,000; ABclonal Technology) were used. Target proteins were detected by an automatic chemiluminescence image analysis system (Tanon, China) through an enhanced chemiluminescence solution (Sparkjade, China). Finally, ImageJ software was used for quantitative analysis.

Cell adhesion assay

The HUVECs (4×10^5 cells/well) were grown in 12-well plates with coverslips placed. After incubating with cytomembrane green fluorescence 3,3′-dioctadecyloxacarbocyanine perchlorate (Dio) dye (Beyotime) in the dark for 20 min, the labeled BMDM (5×10^4/wells) were added to 12-well plates containing HUVECs for co-culture for 1 h. Nonadherent cells were washed with PBS, and then adherent cells were fixed with 4% paraformaldehyde. The prepared samples were observed and photographed using a fluorescence microscope (Olympus IX71).

Transcriptomics

Total RNA was isolated by using the Trizol reagent. Sequencing libraries were constructed, according to the following steps. Firstly, mRNA was purified from total RNA using poly-T oligo-attached magnetic beads. Fragmentation was carried out using divalent cations under elevated temperature in an Illumina proprietary fragmentation buffer. First-strand cDNA was synthesized using random oligonucleotides and Super Script II. Second-strand cDNA synthesis was subsequently performed using DNA polymerase I and RNase H. Remaining overhangs were converted into blunt ends via exonuclease/polymerase activities, and the enzymes were removed. After adenylation of the 3′ ends of the DNA fragments, Illumina PE adapter oligonucleotides were ligated to prepare for hybridization. The sequencing library was then sequenced on NovaSeq 6000 platform (Illumina). Differential expression analysis was performed using the R package "DESeq2." Differential expression genes (DEGs) were identified using specific thresholds: $P < 0.05$. KEGG pathway enrichment analysis of DEGs was performed in R packages "clusterProfiler," "org.Mm.eg.db," and "enrichplot."

Measurement of ATP levels

The BMDM (5×10^6/well) seeded in 6-well plates were treated with both oxLDL (25 μg/mL) and PFOS (0.1 and 1 μM) for 24 h. As previously described (62), the cell supernatant was collected by centrifugation through a cryogenic high-speed centrifuge at 13,000 × *g* for 20 min. According to the manufacturer's instructions, the level of ATP was measured by the ATP assay kit (Beyotime) and normalized in μmol/mg protein.

Target energy metabolomics

Cell samples were sonicated for 20 min at 4 °C in 80% aqueous methanol. Then, after standing at −20 °C for 1 h, the supernatant was obtained by centrifugation at 16,000 × *g* for 20 min at 4 °C. The supernatant was dried by swinging at a high-speed vacuum concentration centrifuge. The samples were redissolved in 40 μL of 50% aqueous methanol and centrifuged at 20,000 × *g*/4 °C for 15 min. The processed samples were separated by Shimadzu Nexera X2 LC-30AD HPLC (Shimazu, Japan). QC samples were inserted into the sample cohort to monitor and evaluate the stability of the system and the reliability of the experimental data. Mass spectrometry was performed using a QTRAP5500 mass spectrometer (AB SCIEX) in positive/negative ion mode. The heat map was plotted by https://www.bioinformatics.com.cn, an online platform for data analysis and visualization.

Measurement of lactate and pyruvate levels

The lactate and pyruvate levels in cell supernatant were measured using commercial kits, according to the corresponding protocols (Nanjing Jiancheng Biological Product, China). Following the addition of collected cell supernatants to the reaction system, optical density values of lactate (530 nm) and pyruvate (505 nm) were measured using a microplate reader (Thermo).

Measurement of glucose uptake

The BMDM (5×10^6/well) seeded in 6-well plates were treated with both oxLDL (25 μg/mL) and PFOS (0.1 and 1 μM) for 24 h. Furthermore, the cells were incubated for 30 min with 20 μM 2-deoxy-2-[(7-nitro-2,1,3-benzoxadiazol-4-yl)amino]-D-glucose (TargetMol, China) working solution. The prepared samples were measured by flow cytometry. The average fluorescence intensity was analyzed using FlowJo (version 10.8.1).

Molecular docking analysis

The interaction pattern between FTH (PDB ID: 4OYN, resolution: 1.43 Å) and 24 PFCs (Table S1) was determined by a flexible molecular docking simulation assay with the AutoDock 4.2 software. The interaction pattern between the FTL (PDB ID: 6WX6, resolution: 2.00 Å) and PFOS was also analyzed. The crystal structure of the protein was obtained from the RCSB Protein Data Bank (http://www.rcsb.org/pdb). In this procedure, water molecules and co-crystal ligands in the crystallin were first removed. The model was then generated and evaluated by AutoGrid. Both ligands and catalytic and iron-storage sites of ferritin were docked using the semi-flexible docking method, respectively. Furthermore, the PyMOL 2.2.0 was applied to visualize the molecular docking results.

MD simulation

MD simulations of the complex of PFOS binding to ferritin were analyzed based on AMber software version 22 (University of California, San Francisco, CA, United States). Initial conformations of FTH and FTL for the MD simulation were taken from the original X-ray diffraction crystal structure and the optimal structure originated from molecular docking, respectively. The ff19SB force field was used for ferritin, and the gaff force field was used for PFOS. The cube TIP3P water model was used for all water boxes, and the minimum distance between the protein and the boundary of the water box was 15 Å. In all complexes, nine Na^+ ions were added to make the system electrically neutral. MD simulations were run with a time length of 100 ns. The binding affinity of PFOS to ferritin was calculated based on the method of molecular mechanics/generalized Born surface area (MM/GBSA). The results of MD simulations were ultimately illustrated by Visual Molecular Dynamics 1.9.3, and the program Discovery Studio

Visualizer 4.0 (Dassault Systèmes, Vélizy-Villacoublay, France) was used to exhibit the patterns of MD simulations.

Measurement of ferrous ion

Briefly, the BMDM (4×10^4/well) was grown in 24-well plates for 12 h. After being treated with PFOS (0.1 and 1 μM) for 24 h, the cells were incubated for 30 min with 1 μM FerroOrange (Dojindo, Japan) working solution configured with HBSS (Gibco). The prepared samples were measured by CytoFLEX flow cytometry (Beckman Coulter Life Sciences, United States) and observed by using a fluorescence microscope (Olympus IX71). The average fluorescence intensity was analyzed using FlowJo (version 10.8.1) and ImageJ (version 1.8.0).

Spectroscopic analysis of conformational changes in FTH

For Fourier infrared exchange spectroscopy, 50 mg/L PFOS and 50 mg/L FTH were incubated at 37 °C for 1 h and then freeze-dried. The lyophilized powder and potassium bromide powder were mixed at a mass ratio of 1:50 and pressed into a mold. The Fourier transform infrared spectroscopy was scanned at a resolution of 32 cm^{-1} and wave numbers ranging from 4,000 to 400 cm^{-1}. For CD analysis, the samples were made by treating 50 mg/L FTH with 50 mg/L PFOS at 37 °C for 45 min. CD spectra of FTH in the presence and absence of PFOS were recorded on a spectropolarimeter (Tokyo, JASCO J-1500, Japan). CD data in the wavelength range of 180–300 nm was collected, and secondary structural changes in FTH upon the binding with PFOS were analyzed using DichroWeb analysis (63).

Machine learning and linear regression assay

The structure–activity relationship was analyzed using the linear regression (LR), decision trees (Tree), support vector regression, random forest, LightGBM, XGBoost, stacking, and artificial neural network machine learning model. The dataset consists of two parts, including the freedom binding affinity of PFCs and FTH, and the PFC structure descriptors from PubChem database (http://pubchem.ncbi.nlm.nih.gov). The machine learning model was trained using the R packages: stats (version 4.3.1), tree (version 1.0.43), e1071 (version 1.7.14), randomForest (version 4.7.1.1), lightgbm (version 4.3.0), xgboost (version 1.7.6.1), caret (version 6.0.94), and neuralnet (version 1.44.2), respectively. The performance of the model was assessed by calculating the root-mean-square error between the predicted and actual values. Moreover, 5-fold cross-validation was used to conduct the test model. Subsequently, the XGBoost model, which exhibited the highest performance in this study, was selected for further investigation (Fig. S13). In this process, the dataset was randomly partitioned into five equivalent subsets, with four subsets allocated for training purposes and the remaining subset reserved for testing. This cross-validation method was applied across diverse datasets to robustly evaluate the model's performance. The 5-fold cross-validation was executed utilizing the R package: caret. Finally, the linear correlation between the key influencing factors (substituent type and carbon chain length of PFCs) and binding affinity was analyzed by LR.

Population experiments section

Study design and population

All participants were from a panel study conducted in Weinan, Shaanxi Province, as details have been described previously (64, 65). Briefly, a total of 142 participants aged 4–12 years were recruited with up to three repeated surveys from 2019 June 3 to 2019 December 27. All participants were relatively healthy and free from infectious and other acute or chronic diseases. After an overnight fast of at least 8 h, all participants donated fasting blood and first-morning urine on the day of health examinations, conducted from 7:30 AM to 9:30 AM in each survey. Well-trained interviewers administered semi-structured questionnaires covering demographic and socioeconomic characteristics, medical history of diseases and medication usage, lifestyle, etc. After excluding the loss of follow-up ($n = 15$ in autumn, $n = 17$ in winter), and missing PFC measurement due to insufficient plasma ($n = 2$ in summer, $n = 6$ in autumn, $n = 5$ in winter), 140 participants with 381 measurements were included in the analysis. The study protocol was approved by the Medical Ethics Committee of the School of Public Health, Tongji Medical College. All subjects and/or their guardians have signed a written informed consent before enrollment.

Determination of plasma PFCs

Concentrations of plasma 11 PFCs were determined by a liquid–liquid extraction coupled with 1,290 ultra-high performance liquid chromatography—6,470 triple quadrupole mass spectrometer under the negative mode (Agilent, United States), including PFOA (>98%), perfluorononanoic acid (PFNA, CAS 375-95-1, >98%), perfluorodecanoic acid (PFDA; CAS 335-76-2, >98%), PFUDA (CAS 2058-94-8, >98%), PFDoA (>98%), perfluorotridecanoic acid (CAS 72629-94-8, >98%), PFOS (>98%), perfluorobutane sulfonic acid (CAS 29420-49-3, >98%), perfluorohexane sulfonate (PFHxS, CAS 82382-12-5, >98%), 6:2 Cl-PFESA (CAS 73606-19-6, >98%), and 8:2 chlorinated polyfluorinated ether sulfonate (8:2 Cl-PFESA, CAS 83329-89-9, >98%) were purchased from Wellington Laboratories (Guelph, Canada). The limit of detection (LOD) was defined as the 3-fold signal-noise ratio (0.01 ng/mL) for 11 PFCs. Concentration below the LOD was replaced by the value of LOD/$\sqrt{2}$. For further analysis, seven PFCs, including PFOA, PFNA, PFDA, PFUDA, PFOS, PFHxS, and 6:2 Cl-PFESA, were included, each with a detection rate of ≥80%.

Atherogenic indices measurements

Fasting blood lipid traits, including TC, TG, high-density cholesterol (HDL-C), and LDL-C, were measured using a CS-400 series automatic biochemical analyzer (DIRUI, China). The atherogenic indices under consideration were the AI and CRI, which were calculated using the following formulas: AI = TC-HDLC/HDLC; CRI = TC/HDLC (66).

Association analysis

Basic characteristics of all participants were presented as median (25th, 75th) for nonnormally distributed continuous variables, and frequency (percentages, %) for categorical variables according to the tertiles of TG levels. Differences in basic characteristics and atherogenic indices were compared using the Kruskal–Wallis test for continuous variables and χ^2 test for categorical variables. Plasma PFC, AI, and CRI were naturally log-transformed for further analysis due to skewed distributions.

LME models with subjects as random intercepts were employed to analyze the associations of individual PFCs with AI and CRI. Adjustments in the model included age, gender, BMI, parental education level, passive smoking status, extra-school activity, season, and dietary variables, including frequency of meat, seafood, packaged food, vegetable, and fruit intake based on previous studies (67, 68). We applied a false discovery rate (FDR) using the

Benjamini–Hochberg correction to correct multiple comparisons, with P-FDR < 0.05 considered statistically significant.

To evaluate the joint effects of plasma PFCs mixture on AI and CRI, we performed WQS regression. Each PFC was assigned a weight expressed as a percentage summing up to one, indicating the relative strength of each compound in the mixture. The model was trained in 40% of the dataset and validated in the remaining 60% of the dataset, with the same covariates adjusted. Based on the 1,000 bootstrap samples, the model was set in positive directions with the hypothesis of a positive relationship between PFCs and AI, CRI.

Meanwhile, a generalized additive model (GAM) with restricted cubic spline was carried out to fit the dose–response associations of PFCs with AI and CRI, treating PFCs as smooth terms and setting the maximum possible degrees of freedom at 4. In addition, after adjusting for other PFCs, we applied multiple PFC LME models to evaluate the associations of different substituent types and carbon chain lengths of PFCs, as identified by the WQS models, with AI and CRI.

The results were expressed as a 1-fold increment of PFCs with the percentage change of AI and CRI ($(e^{(\beta^*\ln 2)}-1)\times 100\%$). Data were analyzed using SAS 9.4 (SAS Institute Inc., United States) and R (version 4.1.2; R Core Team) with "lme4," "gWQS," and "mgcv" packages. The two-sided statistical significance level was set at $P \le 0.05$.

Statistical analysis

The experiments were repeated three times or more, and the data were expressed by mean ± SD. The statistical analysis was performed using GraphPad Prism 9 (GraphPad Software, United States). The significance of the difference between groups was detected by one-way ANOVA. The least significant difference method was used for pairwise comparison when the variance was uniform, and Dunnett's method was used when the variance was corrected. When $P < 0.05$, the difference between groups was statistically significant.

Acknowledgments

Parts of the figure were drawn by using pictures from Servier Medical Art and BioRender.com. Servier Medical Art by Servier is licensed under a Creative Commons Attribution 3.0 Unported License (https://creativecommons.org/licenses/by/3.0/).

Supplementary Material

Supplementary Material is available at *PNAS Nexus* online.

Funding

X.J. is supported in part by the Taishan Scholars Program of Shandong Province (tsqn201909101). X.Z. is supported in part by the National Key Research and Development Program of China (2022YFC3702702). Y.Z. is supported in part by the National Natural Science Foundation of China (82241086).

Author Contributions

Conceptualization: X.J., Z.L., B.Z., and. C.Z. Methodology: Z.L., C.Z., B.Z., H.Y., L.X., Z.H., P.C., and W.P. Investigation: Z.L., Z.Z., B.Z., and C.Z. Visualization: Z.L., Z.Z., B.Z., C.Z., H.Y., and L.X. Supervision: X.J., Y.S., X.Z., and Y.Z. Writing—original draft: Z.L., Z.Z., B.Z., C.Z., H.Y., L.X., P.C., and W.P. Writing—review and editing: X.J., Y.S., X.Z., and Y.Z.

Data Availability

All data are available in the main text or the Supplementary Materials.

References

1 Roth GA, *et al.* 2020. Global burden of cardiovascular diseases and risk factors, 1990–2019: update from the GBD 2019 study. *J Am Coll Cardiol*. 76(25):2982–3021.
2 Libby P, *et al.* 2019. Atherosclerosis. *Nat Rev Dis Primers*. 5(1):56.
3 Raitakari O, Pahkala K, Magnussen CG. 2022. Prevention of atherosclerosis from childhood. *Nat Rev Cardiol*. 19(8):543–554.
4 Libby P. 2021. The changing landscape of atherosclerosis. *Nature*. 592(7855):524–533.
5 Yang B, *et al.* 2022. Evaluation of early biomarkers of atherosclerosis associated with polychlorinated biphenyl exposure: an in vitro and in vivo study. *Environ Health Perspect*. 130(3):37011.
6 Wang Y, Jiang L, Jiang G. 2024. Emerging chemicals in China: historical development, current situation, and future outlook. *Environ Health (Wash)*. 2(4):180–188.
7 Pan XF, Wang LM, Pan A. 2021. Epidemiology and determinants of obesity in China. *Lancet Diabetes Endocrinol*. 9(6):373–392.
8 Chinese Nutrition Society. Scientific research report on dietary guidelines for Chinese residents. 2021. [retrieved 2024 Jun 1]. https://www.chinanutri.cn/yyjkzxpt/yyjkkpzx/yytsg/zgjm/202103/t20210311_224598.html.
9 Unruh D, *et al.* 2015. Red blood cell dysfunction induced by high-fat diet: potential implications for obesity-related atherosclerosis. *Circulation*. 132(20):1898–1908.
10 Shearer JJ, *et al.* 2021. Serum concentrations of per- and polyfluoroalkyl substances and risk of renal cell carcinoma. *J Natl Cancer Inst*. 113(5):580–587.
11 Zhang W, Tian Y, Chen B, Xu S, Wu L. 2024. PFOA/PFOS facilitated intestinal fatty acid absorption by activating the PPARα pathway: insights from organoids model. *Environ Health (Wash)*. 2(2):85–94.
12 Joudan S, Lundgren RJ. 2022. Taking the "F" out of forever chemicals. *Science*. 377(6608):816–817.
13 Lin L-Z, *et al.* 2022. Exposure to per- and polyfluoroalkyl substances and body composition in US adolescents aged 12–18 years: an analysis of data from the National Health and Nutrition Examination Surveys 2011–2018. *Hyg Environ Health Adv*. 3:100009.
14 Xie LN, *et al.* 2022. Serum concentrations of per-/polyfluoroalkyl substances and its association with renal function parameters among teenagers near a Chinese fluorochemical industrial plant: a cross-sectional study. *Environ Pollut*. 302:119020.
15 Christensen BT, Calkins MM. 2023. Occupational exposure to per- and polyfluoroalkyl substances: a scope review of the literature from 1980–2021. *J Expo Sci Environ Epidemiol*. 33(5):673–686.
16 Lind PM, Salihovic S, Stubleski J, Kärrman A, Lind L. 2018. Changes in plasma levels of perfluoroalkyl substances (PFASs) are related to increase in carotid intima-media thickness over 10 years—a longitudinal study. *Environ Health*. 17(1):59.
17 Wen ZJ, Wei YJ, Zhang YF, Zhang YF. 2023. A review of cardiovascular effects and underlying mechanisms of legacy and emerging per- and polyfluoroalkyl substances (PFAS). *Arch Toxicol*. 97(5):1195–1245.
18 Yu XH, Fu YC, Zhang DW, Yin K, Tang CK. 2013. Foam cells in atherosclerosis. *Clin Chim Acta*. 424:245–252.
19 Wolf D, Ley K. 2019. Immunity and inflammation in atherosclerosis. *Circ Res*. 124(2):315–327.

20 Tabas I, Bornfeldt KE. 2016. Macrophage phenotype and function in different stages of atherosclerosis. *Circ Res*. 118(4):653–667.
21 Xu HL, Jiang JX, Chen WZ, Li WL, Chen ZG. 2019. Vascular macrophages in atherosclerosis. *J Immunol Res*. 2019:4354786.
22 Ruan CF, *et al*. 2022. Matrix thermal shift assay for fast construction of multidimensional ligand-target space. *Anal Chem*. 94(17): 6482–6490.
23 Theil EC. 1987. Ferritin: structure, gene regulation, and cellular function in animals, plants, and microorganisms. *Annu Rev Biochem*. 56:289–315.
24 Plays M, Müller S, Rodriguez R. 2021. Chemistry and biology of ferritin. *Metallomics*. 13(5):mfab021.
25 Honarmand Ebrahimi K, Bill E, Hagedoorn P-L, Hagen WR. 2012. The catalytic center of ferritin regulates iron storage via Fe(II)-Fe(III) displacement. *Nat Chem Biol*. 8(11):941–948.
26 Hamid N, *et al*. 2023. An integrated assessment of ecological and human health risks of per- and polyfluoroalkyl substances through toxicity prediction approaches. *Sci Total Environ*. 905:167213.
27 Li LH, *et al*. 2022. Comprehensive exposure studies of per- and polyfluoroalkyl substances in the general population: target, nontarget screening, and toxicity prediction. *Environ Sci Technol*. 56(20):14617–14626.
28 Perdomo L, *et al*. 2020. Large extracellular vesicle-associated Rap1 accumulates in atherosclerotic plaques, correlates with vascular risks and is involved in atherosclerosis. *Circ Res*. 127(6):747–760.
29 van Gils JM, *et al*. 2012. The neuroimmune guidance cue netrin-1 promotes atherosclerosis by inhibiting the emigration of macrophages from plaques. *Nat Immunol*. 13(2):136–143.
30 Finn AV, *et al*. 2012. Hemoglobin directs macrophage differentiation and prevents foam cell formation in human atherosclerotic plaques. *J Am Coll Cardiol*. 59(2):166–177.
31 Eckel RH, Grundy SM, Zimmet PZ. 2005. The metabolic syndrome. *Lancet*. 365(9468):1415–1428.
32 Wu Q, Gao ZJ, Yu X, Wang P. 2022. Dietary regulation in health and disease. *Signal Transduct Target Ther*. 7(1):252.
33 Powell-Wiley TM, *et al*. 2021. Obesity and cardiovascular disease: a scientific statement from the American Heart Association. *Circulation*. 143(21):e984–e1010.
34 Ford ES, Li C, Zhao G, Pearson WS, Mokdad AH. 2009. Hypertriglyceridemia and its pharmacologic treatment among US adults. *Arch Intern Med*. 169(6):572–578.
35 Kobiyama K, Ley K. 2018. Atherosclerosis: a chronic inflammatory disease with an autoimmune component. *Circ Res*. 123(10): 1118–1120.
36 Engelen SE, Robinson AJB, Zurke YX, Monaco C. 2022. Therapeutic strategies targeting inflammation and immunity in atherosclerosis: how to proceed? *Nat Rev Cardiol*. 19(8):522–542.
37 Li Y, *et al*. 2023. Macrophage P2Y6 receptor deletion attenuates atherosclerosis by limiting foam cell formation through phospholipase Cβ/store-operated calcium entry/calreticulin/scavenger receptor A pathways. *Eur Heart J*. 45(4):268–283.
38 Luo YT, *et al*. 2017. Macrophagic CD146 promotes foam cell formation and retention during atherosclerosis. *Cell Res*. 27(3):352–372.
39 Kanneganti TD, Dixit VD. 2012. Immunological complications of obesity. *Nat Immunol*. 13(8):707–712.
40 Tabas I, Bornfeldt KE. 2020. Intracellular and intercellular aspects of macrophage immunometabolism in atherosclerosis. *Circ Res*. 126(9):1209–1227.
41 Wen JQ, *et al*. 2023. Diversity of arterial cell and phenotypic heterogeneity induced by high-fat and high-cholesterol diet. *Front Cell Dev Biol*. 11:971091.
42 Van den Bossche J, O'Neill LA, Menon D. 2017. Macrophage immunometabolism: where are we (going)? *Trends Immunol*. 38(6):395–406.
43 Xie M, *et al*. 2016. PKM2-dependent glycolysis promotes NLRP3 and AIM2 inflammasome activation. *Nat Commun*. 7:13280.
44 Shirai T, *et al*. 2016. The glycolytic enzyme PKM2 bridges metabolic and inflammatory dysfunction in coronary artery disease. *J Exp Med*. 213(3):337–354.
45 Millet P, Vachharajani V, McPhail L, Yoza B, McCall CE. 2016. GAPDH binding to TNF-α mRNA contributes to posttranscriptional repression in monocytes: a novel mechanism of communication between inflammation and metabolism. *J Immunol*. 196(6): 2541–2551.
46 Yan JW, Horng T. 2020. Lipid metabolism in regulation of macrophage functions. *Trends Cell Biol*. 30(12):979–989.
47 Glass CK, Witztum JL. 2001. Atherosclerosis. The road ahead. *Cell*. 104(4):503–516.
48 Yu HY, *et al*. 2022. The foam cell formation associated with imbalanced cholesterol homeostasis due to airborne magnetite nanoparticles exposure. *Toxicol Sci*. 189(2):287–300.
49 Zhang JX, *et al*. 2023. Airborne magnetite nanoparticles induced early vascular pathologies by disrupting lipid metabolism under high-fat dietary patterns. *Environ Toxicol*. 39(3):1175–1186.
50 Grabner GF, Xie H, Schweiger M, Zechner R. 2021. Lipolysis: cellular mechanisms for lipid mobilization from fat stores. *Nat Metab*. 3(11):1445–1465.
51 Rodríguez-Prados JC, *et al*. 2010. Substrate fate in activated macrophages: a comparison between innate, classic, and alternative activation. *J Immunol*. 185(1):605–614.
52 Goicoechea L, Conde de la Rosa L, Torres S, García-Ruiz C, Fernández-Checa JC. 2023. Mitochondrial cholesterol: metabolism and impact on redox biology and disease. *Redox Biol*. 61:102643.
53 Karunakaran D, *et al*. 2015. Macrophage mitochondrial energy status regulates cholesterol efflux and is enhanced by anti-miR33 in atherosclerosis. *Circ Res*. 117(3):266–278.
54 Xia YY, *et al*. 2021. Ironing out the details: how iron orchestrates macrophage polarization. *Front Immunol*. 12:669566.
55 Liu ZL, *et al*. 2023. Iron promotes glycolysis to drive colon tumorigenesis. *Biochim Biophys Acta Mol Basis Dis*. 1869(8):166846.
56 Amstutz VH, Cengo A, Gehres F, Sijm DTHM, Vrolijk MF. 2022. Investigating the cytotoxicity of per- and polyfluoroalkyl substances in HepG2 cells: a structure-activity relationship approach. *Toxicology*. 480:153312.
57 Nowacki A, Sikora K, Dmochowska B, Wisniewski A. 2013. DFT studies of the conversion of four mesylate esters during reaction with ammonia. *J Mol Model*. 19(8):3015–3026.
58 Milnes-Smith E, Stone CA, Willis CR, Perkin S. 2022. Surface reconstruction of fluoropolymers in liquid media. *Langmuir*. 38(16):4657–4668.
59 Wan HT, *et al*. 2021. Characterization of PFOS toxicity on in-vivo and ex-vivo mouse pancreatic islets. *Environ Pollut*. 289:117857.
60 Jin XT, *et al*. 2022. Exogenous chemical exposure increased transcription levels of the host virus receptor involving coronavirus infection. *Environ Sci Technol*. 56(3):1854–1863.
61 Liu K, *et al*. 2015. Impaired macrophage autophagy increases the immune response in obese mice by promoting proinflammatory macrophage polarization. *Autophagy*. 11(2):271–284.
62 Nayak MK, *et al*. 2021. The metabolic enzyme pyruvate kinase M2 regulates platelet function and arterial thrombosis. *Blood*. 137(12):1658–1668.
63 Miles AJ, Ramalli SG, Wallace BA. 2022. DichroWeb, a website for calculating protein secondary structure from circular dichroism spectroscopic data. *Protein Sci*. 31(1):37–46.
64 Liu M, *et al*. 2021. Association of personal fine particulate matter and its respiratory tract depositions with blood

pressure in children: from two panel studies. *J Hazard Mater*. 416: 126120.

65 Liu M, *et al.* 2022. Co-exposure to priority-controlled metals mixture and blood pressure in Chinese children from two panel studies. *Environ Pollut*. 306:119388.

66 Markelic I, *et al.* 2021. Lipid profile and atherogenic indices in patients with stable chronic obstructive pulmonary disease. *Nutr Metab Cardiovasc Dis*. 31(1):153–161.

67 Papadopoulou E, *et al.* 2019. Diet as a source of exposure to environmental contaminants for pregnant women and children from six European countries. *Environ Health Perspect*. 127(10): 107005.

68 Poothong S, Papadopoulou E, Padilla-Sánchez JA, Thomsen C, Haug LS. 2020. Multiple pathways of human exposure to poly- and perfluoroalkyl substances (PFASs): from external exposure to human blood. *Environ Int*. 134:105244.